Enhancement of second harmonic generation in one-dimensional nonlinear photonic-crystal microcavities

Jinan Xia

*Materials and Microsystems Laboratory (χLab), Politecnico di Torino,
corso Duca degli Abruzzi 24, 10129 Torino, Italy*
jinan.xia@polito.it

Abstract: A numerical iteration technique starting from the analytical solution of the fundamental wave and the second harmonic wave propagation equations in undepleted-pump approximation is presented for analysis of second harmonic generation in one-dimensional nonlinear photonic-crystal microcavities under pump light incidence at an arbitrary angle, accounting for pump depletion. Numerical results are in good agreement with experimental observation and theoretical predication by transfer matrix method. Analysis of the conversion efficiency of second harmonic generation in nonlinear photonic-crystal microcavities shows that dramatic enhancement of second harmonic generation occurs in the microcavities which have the optimal numbers of distributed Bragg reflector layers. The enhancement of nonlinear interactions is ascribed to mode resonance and localization of high intensity fundamental field, corresponding to the defect mode within the forbidden band of the photonic-crystal microcavities.

References and links

1. I. V. Soboleva, E. M. Murchikova, A. A. Fedyanin, and O. A. Aktsipetrov, "Second- and third-harmonic generation in birefringent photonic crystals and microcavities based on anisotropic porous silicon," Appl. Phys. Lett. **87**(24), 241110 (2005).
2. S. Lettieri, S. D. Finizio, P. Maddalena, V. Ballarini, and F. Giorgis, "Second-hamonic generation in amorphous silicon nitride microcavities," Appl. Phys. Lett. **81**(25), 4706 (2002).
3. W. Nakagawa, R. C. Tyan, and Y. Fainman, "Analysis of enhanced second-harmonic generation in periodic nanostructures using modified rigorous coupled-wave analysis in the undepleted-pump approximation," J. Opt. Soc. Am. A **19**(9), 1919–1928 (2002).
4. T. Ochiai, and K. Sakoda, "Scaling law of enhanced second harmonic generation in finite Bragg stacks," Opt. Express **13**(22), 9094–9114 (2005).
5. J. J. Li, Z. Y. Li, and D. Z. Zhang, "Second harmonic generation in one-dimensional nonlinear photonic crystals solved by the transfer matrix method," Phys. Rev. E Stat. Nonlin. Soft Matter Phys. **75**(5), 056606 (2007).
6. M. F. Saleh, L. Dal Negro, and B. E. Saleh, "Second-order parametric interactions in 1-D photonic-crystal microcavity structures," Opt. Express **16**(8), 5261–5276 (2008).
7. S. Enoch, and H. Akhouayri, "Second-harmonic generation in multilayered devices: theoretical tools," J. Opt. Soc. Am. B **15**(3), 1030–1041 (1998).
8. G. D'Aguanno, M. Centini, M. Scalora, C. Sibilia, M. Bertolotti, M. J. Bloemer, and C. M. Bowden, "Generalized coupled-mode theory for $\chi^{(2)}$ interactions in finite multilayered structures," J. Opt. Soc. Am. B **19**(9), 2111–2121 (2002).
9. L. Zhao, and B. Gu, "Giant enhancement of second harmonic generation in multiple photonic quantum well structures made of nonlinear material," Appl. Phys. Lett. **88**(12), 122904 (2006).
10. T. V. Dolgova, A. I. Maidykovski, M. G. Martemyanov, A. A. Fedyanin, O. A. Aktsipetrov, G. Marowsky, V. A. Yakovlev, G. Mattei, N. Ohta, and S. Nakabayashi, "Giant optical second-harmonic generation in single and coupled microcavities formed from one-dimensional photonic crystals," J. Opt. Soc. Am. B **19**(9), 2129–2140 (2002).
11. V. Y. Timoshenko, L. A. Osminkina, A. I. Efimova, L. A. Golovan, P. K. Kashkarov, D. Kovalev, N. Kunzner, E. Gross, J. Diener, and F. Koch, "Anisotropy of optical absorption in birefringent porous silicon," Phys. Rev. B **67**(11), 113405 (2003).

12. T. V. Dolgova, A. I. Maidikovskii, M. G. Martem'yanov, G. Marovsky, G. Mattei, D. Schuhmacher, V. A. Yakovlev, A. A. Fedyanin, and O. A. Aktsipetrov, "Giant second harmonic generation in microcavities based on porous silicon photonic crystals," JETP Lett. **73**(1), 6–9 (2001).
13. T. V. Dolgova, A. I. Maidykovski, M. G. Martemyanov, A. A. Fedyanin, O. A. Aktsipetrov, G. Marowsky, V. A. Yakovlev, and G. Mattei, "Giant microcavity enhancement of second-harmonic generation in all-silicon photonic crystals," Appl. Phys. Lett. **81**(15), 2725 (2002).
14. J. Trull, R. Vilaseca, J. Martorell, and R. Corbalan, "Second-harmonic generation in local modes of a truncated periodic structure," Opt. Lett. **20**(17), 1746–1748 (1995).
15. L. M. Zhao, and B. Y. Gu, "Enhanced second-harmonic generation for multiple wavelengths by defect modes in one-dimensional photonic crystals," Opt. Lett. **31**(10), 1510–1512 (2006).

1. Introduction

Second- and third- harmonic generation have been realized in one-dimensional nonlinear photonic crystal microcavities [1,2]. To analyze the nonlinear optical properties of one-dimensional photonic crystal structures, a number of mathematical methods, for instance, the rigorous coupled-wave analysis [3], the Green function method [4], and the transfer matrix method [5] have been developed. As previously pointed out [6], most of the methods are limited by certain requirements and assumptions such as the use of the undepleted pump approximation and the requirement that the interacting waves propagate along the normal axis of the structure, while normal incidence may inhibit second-order nonlinear process for some photonic crystal structures. To circumvent the limitations, a model based on the transfer matrix method for studying second harmonic generation and optical parametric amplification in 1-D multilayered photonic crystal structures was presented [6], accounting for collinear oblique waves and pump depletion.

In this work, second harmonic generation of one-dimensional nonlinear photonic-crystal microcavities is analyzed by solving the fundamental wave (FW) and the second harmonic wave (SHW) propagation equations. It is emphasized that both the analytical solution of wave propagation equations in undepleted-pump approximation and the numerically iterative solution in depleted pump can be obtained for pump light incidence at an arbitrary angle without limitation of incident light propagating along the normal axis of a photonic crystal. It will be shown that the conversion efficiency of second harmonic generation in a one-dimensional photonic crystal microcavity strongly depends on the photonic crystal structure and optical property of the crystal material. High conversion efficiency of second harmonic generation could be achieved for the optimal pair numbers of DBRs in a photonic crystal microcavity.

2. Coupled-wave equations and solutions

The typical microcavity (MC) studied is shown in Fig. 1. It consists of top and bottom distributed Bragg reflectors (DBRs) separated by a cavity spacer. Each Bragg reflector is made up of a stack of high and low refractive index alternating layers with optical thickness of a quarter wavelength. An incident plane wave at fundamental frequency ω impinges on the sample at an angle of incidence θ_0. Considering the case of a plane incident wave at TE polarization, the equations governing nonlinear quadratic interactions of two monochromatic plane waves at the fundamental frequency and the second harmonic (SH) frequency inside each layer of the microcavity can be written as [7,8],

$$\frac{d^2 E_y^{(1)}}{dz^2} + \beta^{(1)2} E_y^{(1)} = -2k_{10}^2 \chi^{(2)} E_y^{*(1)} E_y^{(2)}, \tag{1}$$

$$\frac{d^2 E_y^{(2)}}{dz^2} + \beta^{(2)2} E_y^{(2)} = -k_{20}^2 \chi^{(2)} E_y^{(1)2}, \tag{2}$$

$$\beta^{(1)} = \left[k^{(1)2} - k_0^{(1)2} \sin^2 \theta_0^{(1)} \right]^{\frac{1}{2}}, \quad \beta^{(2)} = \left[k^{(2)2} - k_0^{(2)2} \sin^2 \theta_0^{(2)} \right]^{\frac{1}{2}}, \tag{3}$$

where $E_y^{(1)}$, $E_y^{(2)}$ are the electric fields of the fundamental wave and the second harmonic wave along the y-direction, the superscript (1) refers to the fundamental wave, the superscript (2) refers to the second harmonic wave, the superscript * represents the complex conjugate. y-axis is perpendicular to xz-plane. $k^{(1)} = n^{(1)}k_{10}$, and $k^{(2)} = n^{(2)}k_{20}$ are the wave vectors of the FW and the SHW, respectively. $k_{10} = \omega/c$, and $k_{20} = 2\omega/c$. ω is the angular frequency of the FW, c is the light speed in vacuum. $n^{(1)}$ ($n^{(2)}$) is the refractive index of the layered material at the FW (SHW) frequency. The refractive index of the material in a layer of the microcavity at a wavelength is assumed to be same, but the refractive index is different for different layer. $k_0^{(1)} = n_0^{(1)}k_{10}$, and $k_0^{(2)} = n_0^{(2)}k_{20}$ are the wave vectors of the FW and SHW in the incident medium. $n_0^{(1)}$ ($n_0^{(2)}$) is the refractive index of the incident medium at the FW (SHW) frequency. $\chi^{(2)}$ is the spatially dependent quadratic effective nonlinear coefficient. $\theta_0^{(1)}$, $\theta_0^{(2)}$ are the incident angles of FW and SHW on the MC structure.
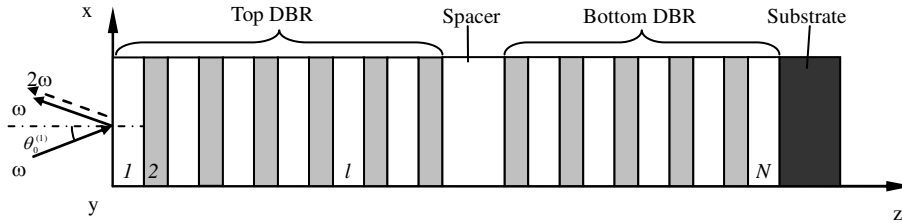

Fig. 1. Schematic of a MC structure, showing the coordinate axes and incident angles. White block: low index layer; grey block: high index layer.

The solution of Eq. (1) can be written as

$$E_{y,l}^{(1)}(z) = E_{undepleted,l}^{(1)}(z) + E_{p,l}(z), \qquad (4)$$

$$E_{undepleted,l}^{(1)}(z) = A_{undepleted,l}^{(1)}e^{j\beta_l^{(1)}(z-z_{l-1})} + B_{undepleted,l}^{(1)}e^{-j\beta_l^{(1)}(z-z_{l-1})}, \qquad (5)$$

where the subscript l refers to the l-th layer. $E_{y,l}^{(1)}(z)$ is the FW electrical field along the y-direction at z position in the l-th layer, $E_{undepleted,l}^{(1)}(z)$ is the FW electrical field along the y-direction at z position in the l-th layer under undepleted pump approximation and it is the solution of the equation as follows:

$$\frac{d^2E_y^{(1)}}{dz^2} + \beta^{(1)2}E_y^{(1)} = 0. \qquad (6)$$

$A_{undepleted,l}^{(1)}$ and $B_{undepleted,l}^{(1)}$, respectively, represent the electric field amplitudes of the backward and forward FW at the interface between two layers under undepleted pump approximation. By matching the tangential electric- and magnetic-field components at the boundaries between the layers, the same method in [9] can be used to find the electric field amplitudes $A_{undepleted,l}^{(1)}$ and $B_{undepleted,l}^{(1)}$ of each layer under the initial condition: $A_{undepleted,N}^{(1)} = 0$, $B_{undepleted,1}^{(1)} = \sqrt{2I_0 / \varepsilon_0 c n_0^{(1)}}$, where I_0 is the intensity of the incident laser beam, ε_0 the permittivity of vacuum.

From the viewpoint of mathematics, $E_{p,l}(z)$ is the particular solution of Eq. (1). Since the term on the right hand side of Eq. (1) is very small, we regard that the particular solution $E_{p,l}(z)$ is the perturbation of the FW electrical field when depleted pump is taken into account. If the term on the right hand side of Eq. (1) is constant, the particular solution $E_{p,l}(z)$ can be obtained from Eq. (1) as

$$E_{p,l}(z) = -\frac{2k_{10}^2 \chi_l^{(2)} E_{y,l}^{*(1)}(z) E_{y,l}^{(2)}(z)}{\beta_l^{(1)2}} = -\frac{2\chi_l^{(2)} E_{y,l}^{*(1)}(z) E_{y,l}^{(2)}(z)}{\left[n_l^{(1)2} - n_0^{(1)2} \sin^2 \theta_0^{(1)} \right]}. \tag{7}$$

Substituting Eq. (7) and Eq. (5) into Eq. (4), we obtain

$$E_{y,l}^{(1)}(z) = A_l^{(1)} e^{j\beta_l^{(1)}(z-z_{l-1})} + B_l^{(1)} e^{-j\beta_l^{(1)}(z-z_{l-1})}, \tag{8}$$

$$A_l^{(1)} = (1+\Delta) A_{undepleted,l}^{(1)}, \quad B_l^{(1)} = (1+\Delta) B_{undepleted,l}^{(1)}, \tag{9}$$

$$\Delta = -\frac{2\chi_l^{(2)} E_{y,l}^{*(1)}(z) E_{y,l}^{(2)}(z)}{\left[n_l^{(1)2} - n_0^{(1)2} \sin^2 \theta_0^{(1)} \right] E_{undepleted,l}^{(1)}(z)}, \tag{10}$$

where $A_l^{(1)}$ and $B_l^{(1)}$ are the electric field amplitudes of the backward and forward FWs at the interface under depleted pump, respectively.

From Eq. (2), the SHW electric field can be expressed as

$$E_{y,l}^{(2)} = A_l^{(2)} e^{j\beta_l^{(2)}(z-z_{l-1})} + B_l^{(2)} e^{-j\beta_l^{(2)}(z-z_{l-1})}$$
$$+ C_{21} e^{j2\beta_l^{(1)}(z-z_{l-1})} + C_{22} e^{-j2\beta_l^{(1)}(z-z_{l-1})} - \frac{2k_{20}^2 \chi_l^{(2)}}{\beta_l^{(2)2}} A_l^{(1)} B_l^{(1)}, \tag{11}$$

$$C_{21} = \frac{-k_{20}^2 \chi_l^{(2)} A_l^{(1)2}}{\beta_l^{(2)2} - 4\beta_l^{(1)2}}, \quad C_{22} = \frac{-k_{20}^2 \chi_l^{(2)} B_l^{(1)2}}{\beta_l^{(2)2} - 4\beta_l^{(1)2}}. \tag{12}$$

Considering the initial conditions: $A_N^{(2)} = 0$, $B_1^{(2)} = 0$, the coefficients $A_l^{(2)}$ and $B_l^{(2)}$ can be determined by using the same method in [9] and the continuous condition of the electric and magnetic fields at the interface between two layers.

Equation (7) is approximately the particular solution of Eq. (1), because the term on the right hand side of Eq. (1) is not constant and it is the function of FW and SHW fields. We had to find the precision value of the particular solution by using numerical iteration, so that we can obtain the precision solutions of FW and SHW fields for Eq. (1) and Eq. (2). For the complete computation procedure, it is based on two-step process. At first, use Eq. (6) and Eq. (2) to find their solutions Eq. (5) and Eq. (11) under undepleted pump approximation as doing in [9], while the parameters β which account for the incident angle of pump beam are used to replace the parameters k in the reference. Second, the solutions of FW and SHW under undepleted pump approximation are used as the initial values to find perturbation $E_{p,l}(z)$ by numerical iteration. The two-step process can be described in detail as follows:

First, find the coefficients $A_{undepleted,l}^{(1)}$, $B_{undepleted,l}^{(1)}$ in Eq. (5) and the solution Eq. (5) of Eq. (6) by matching the FW tangential electric- and magnetic-field components at the boundaries between the layers. Substitute $A_{undepleted,l}^{(1)}$, $B_{undepleted,l}^{(1)}$ as $A_l^{(1)}$, $B_l^{(1)}$ into Eq. (12) and Eq. (11). Apply Eq. (11) to find the coefficients $A_l^{(2)}$, $B_l^{(2)}$, and the electrical fields of SHWs under undepleted pump approximation by using the continuous condition of the SHW electric and magnetic fields at the interface between the layers. Second, the solutions for FW and SHW electrical fields are substituted into Eqs. (10) and Eq. (9) to calculate the electric field amplitudes of the backward and forward FWs: $A_l^{(1)}$ and $B_l^{(1)}$. Third, $A_l^{(1)}$ and $B_l^{(1)}$ are substituted into Eq. (12) so as to calculate coefficients C_{21} and C_{22}. Use Eq. (11) and the continuous condition of the SHW electric and magnetic fields at the interface between the layers to determine the coefficients $A_l^{(2)}$ and $B_l^{(2)}$. Compute the spatial distributions of the electric and magnetic fields of FW and SHW inside each layer. Monitor the convergence condition: Eq. (13). Fourth, repeat the second and the third step until the convergence is reached.

We consider the convergence condition as

$$\frac{\left| I_{z,new}^{(2)} - I_z^{(2)} \right|}{I_z^{(2)}} \leq Err, \tag{13}$$

where $I_{z,new}^{(2)}$ and $I_z^{(2)}$ are new and previous intensities of the SHW fields at z-position during the iteration. *Err* is an infinitesimal value to control convergence for the iteration.

The conversion efficiencies of forward and backward waves are evaluated by [6]

$$\eta_{forth} = \frac{I_{forth,N}^{(2)}}{I_0}, \quad \eta_{back} = \frac{I_{back,1}^{(2)}}{I_0}, \tag{14}$$

where $I_{forth,N}^{(2)}$ and $I_{back,1}^{(2)}$ are the output intensities of the forward SHW in the last layer and the backward SHW in the first layer.

For a plane incident wave at TM polarization, the equations governing nonlinear quadratic interactions of two monochromatic plane waves at the fundamental frequency and second harmonic frequency in the microcavity can be written as [7],

$$\frac{d^2 H_y^{(1)}}{dz^2} + \beta^{(1)2} H_y^{(1)} = -j\omega rot(\mathbf{P}_{NL}^{(1)}) \cdot \hat{\mathbf{y}}, \tag{15}$$

$$\frac{d^2 H_y^{(2)}}{dz^2} + \beta^{(2)2} H_y^{(2)} = -2j\omega rot(\mathbf{P}_{NL}^{(2)}) \cdot \hat{\mathbf{y}}, \tag{16}$$

where $H_y^{(1)}$, $H_y^{(2)}$ are the magnetic fields of the fundamental wave and the second harmonic wave along y-direction. $\mathbf{P}_{NL}^{(1)}$, $\mathbf{P}_{NL}^{(2)}$ are nonlinear polarizations at the fundamental wave frequency and the harmonic frequency. *rot* refers to curl. $\hat{\mathbf{y}}$ refers to the unit vector along y-direction. After simplifying the expressions of the curls of the nonlinear polarizations $\mathbf{P}_{NL}^{(1)}$ and $\mathbf{P}_{NL}^{(2)}$, the similar method above can be used to calculate the magnetic fields of FW and SHW in the crystal structures.

3. Numerical results and discussion

To confirm the validity of the numerical method, the FW and SHG intensities are compared with the experimental and numerical results for an anisotropic porous silicon photonic crystal Fabry-Perot microcavity reported in [10]. Note that silicon crystal is isotropic, but porous modification of silicon can exhibit strong in-plane anisotropy of the refractive index due to shape anisotropy of Si nanocrystals and voids assembling the material reported in [1,11]. The MC composes of two distributed Bragg reflectors (DBRs) separated by a MC spacer with an optical thickness of $\lambda_{MC}/2$. Its cavity mode centers at $\lambda_{MC} = 0.945$ μm for normal incidence. The bottom DBR consists of 5 pairs of $\lambda_{MC}/4$-thick porous silicon layers with high and low refractive indices $n_H = 1.41$ and $n_L = 1.18$ at the wavelength of 0.945 μm, corresponding to porosities of $f_H = 0.77$ and $f_L = 0.88$, respectively. The top DBR has 5.5 pairs of $\lambda_{MC}/4$-thick porous silicon layers. A low-refractive-index $\lambda_{MC}/2$-thick porous silicon layer is on top of the MC. The spacer of MC has a refractive index of 1.18 at 0.945 μm, corresponding to the porosity of $f_L = 0.88$. The substrate of the microcavity has refractive indices of 3.75 at 0.945 μm and 4.47 at 0.473 μm. The refractive indices of high and low index layers in DBRs of the MC are 1.47 and 1.2 at the wavelength of 0.473 μm, respectively. The second order effective nonlinear coefficients are assumed to be 20 and 10 pm/V for high and low index layers. The pump laser pulses have the duration of 4 ns, the energy of 10 mJ, and the spot diameter of 1 mm on the surface of the MC. In the simulation, we assume that SHG in the porous silicon-based photonic crystal Fabry-Perot microcavity is mainly ascribed to the nonlinear properties

of the anisotropic porous silicon, and neglect the contribution of surface nonlinear interaction at layer interfaces to SHG since the surface nonlinear coefficients are much smaller than the nonlinear coefficients from the shape anisotropy of Si nanocrystals and voids in the porous silicon photonic crystals. In addition, we use a dominating nonlinear coefficient in a polarization direction as the quadratic effective nonlinear coefficient in the nonlinear equations to analyze the nonlinear phenomenon and neglect the anisotropic effect of the nonlinear coefficients on SHG in other polarization directions, because the strongest SHW is produced in the polarization direction corresponding to the largest nonlinear coefficient of a nonlinear material in the photonic crystal structure and weaker SHW is produced in other direction if the pump light is set to irradiate on the nonlinear photonic crystal along a special direction.

Considering s-polarized FW pump and p-polarized SH radiation as doing in [10], the calculated SHW intensity spectra of the MC are shown in Fig. 2. It is seen that the SHW intensity is strongly enhanced at $\lambda_\omega = 0.783$ μm for $\theta_0 = 45°$, $\lambda_\omega \approx 813$ μm for $\theta_0 = 40°$, and $\lambda_\omega \approx 868$ μm for $\theta_0 = 30°$. The reason is that these fundamental wave fields are in resonance with the cavity modes at the incident angles. Two other spectral features at $\lambda_\omega = 0.913$ μm for $\theta_0 = 45°$ and at $\lambda_\omega = 0.944$ μm for $\theta_0 = 40°$, respectively, correspond to both photonic bandgap edges. These are in good agreement with the reported numerical results based on transfer matrix method and are in good qualitative agreement with experimental measurement in [10,12,13]. This indicates that current numerical method is valid to simulate the FW and SHW fields in the photonic crystal structures.
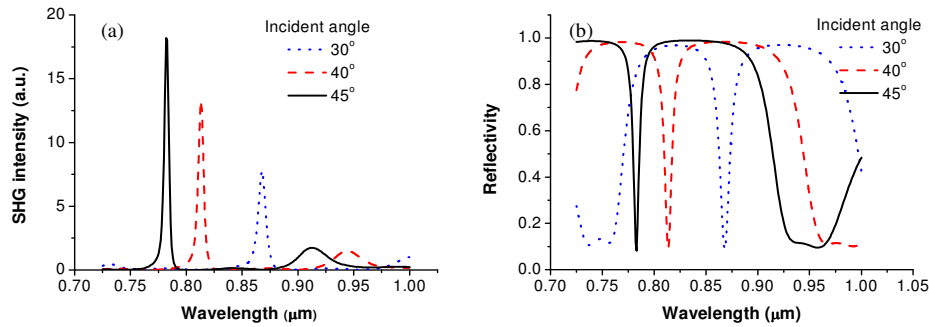

Fig. 2. (a). Intensity of backward SH radiation as a function of wavelength for s-polarized fundamental wave at different angles of incidence: $\theta_0 = 45°$, 40 °, and 30 °. (b) The linear reflection spectra for the s-polarized fundamental wave at different angles of incidence: $\theta_0 = 45°$, 40 °, and 30 °.

Let us examine the SHG in the microcavities shown in Fig. 1. Suppose that the microcavity spacer layers have optical thicknesses of $\lambda_{MC}/2$. Simulated results showed that the conversion efficiency of second harmonic generation was exponentially dependent on the number of photonic crystal layers for a symmetrical photonic crystal microcavity consisting of alternating layers of a nonlinear material GaN and air. Simulated results also showed that all of backward SHG, forward SHG, and total SHG conversion efficiencies increased almost linearly with increasing the pump intensity in the GaN and air photonic crystal microcavity. These results are in good agreement with the reported in [6]. However, the conversion efficiency of second harmonic generation does not always increase with the layer number for other photonic crystal microcavity structures. Consider the MCs made of nonlinear materials instead of porous silicon. We assume that the nonlinear materials have the same nonlinear coefficients and refractive indices in high and low index layers as those in high and low index porous silicon layers mentioned above. We set that the pair numbers of top DBRs in the MCs are 12. The pump laser pulses have the energy of 20 mJ, the duration of 4 ns, the spot diameter of 1 mm, and the incident angle of 45°. Set s-polarized FW pump and p-polarized SH radiation for the microcavities. As shown in Fig. 3, several peaks are seen, corresponding

to the backward SHG conversion efficiencies of 11.11%, 11.99%, 11.51%, 11.98% (forward SHG conversion efficiencies of 4.33%, 4.64%, 4.64%, 4.59%) at the pair numbers of bottom DBRs: 15, 26, 37, 47, respectively.

The peak conversion efficiencies in Fig. 3 originate from the fact that the FWs are located at the defect modes within the forbidden bands of the photonic crystal MCs and that they are in resonance with cavity modes [14,15], resulting in high intensity FW fields confined in the spacer layers of the MCs. As can be seen in Fig. 4(a), the peaks of FW field intensities are confined and located at the centers of the spacer layers in the MCs. On the other hand, due to the optimal numbers of the DBR layers for the pump light incidence, the FW intensity in the MC is dramatically enhanced, because the most efficient FW coupling into cavity modes in the MCs is achieved. It is seen in Fig. 4(a) that the field intensity of FW in the spacer layer for the MC with top and bottom DBRs consisting of 12 and15 pairs of high and low index layers are much higher than the FW field intensities in the MCs with top and bottom DBRs consisting of 14, 15 pairs and 19, 15 pairs of high and low index layers. The high intensity FWs in spacer layers enhance the second order nonlinearity. Figure 4(b) shows that the field intensity of SHW in the MC with top and bottom DBRs consisting of 12 and 15 pairs of high and low index layers are much higher than the SHW field intensities in two other MCs.
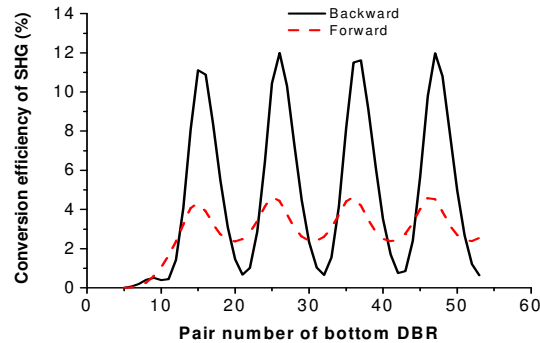

Fig. 3. Efficiencies of backward SHG (solid line) and forward SHG (dashed line) as a function of pair number of bottom DBR in the MC for s-polarized pump incidence at the wavelength of 0.783 μm and the angle of incidence: $\theta_0 = 45°$, top DBRs consisting of 12 pairs of high and low index layers.
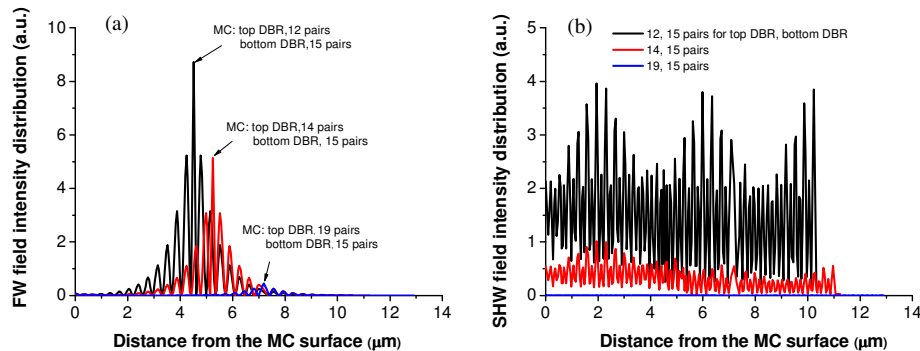

Fig. 4. (a). Electrical field intensity distribution of FWs in the MCs for the s-polarized pump incidence at the wavelength of 0.783 μm and the angle of incidence: $\theta_0 = 45°$. The peaks are located at the centers of the spacer layers in the MCs. (b) Electrical field intensity distribution of SHWs.

Figure 5 reports the wavelength dependence of backward and forward SHG conversion efficiencies in a MC which consists of 12 and 15 pairs of alterative index layers in top and

bottom DBRs at the pump pulses of 20 mJ, 4 ns, the spot diameter of 1 mm, and the angle of incidence of $\theta_0 = 45°$. The refractive indices and nonlinear coefficients of the materials are the same as those in Fig. 3 and Fig. 4. Insert is the reflection spectrum of the MC, indicating a defect mode at the wavelength of 0.783 μm. Due to the resonance of the FW with cavity mode, the conversion efficiency of SHG at the resonant wavelength is dramatically increased. As can be seen, when the cavity is pumped at the resonant wavelength of 0.783 μm, the conversion efficiencies of backward SHG and forward SHG are 11.2%, and 4.3%, respectively, which are about 10^4 times of the SH conversion efficiencies from the pump light at wavelengths outside the resonant wavelength.
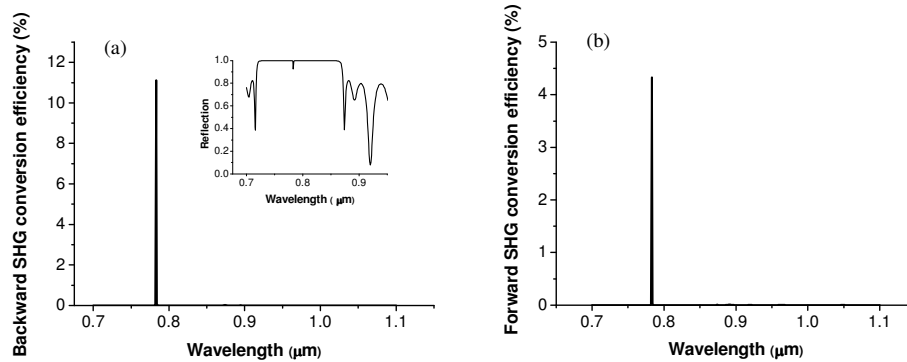

Fig. 5. Wavelength dependence of SHG conversion efficiency of the MC consisting of 12 and 15 pairs of high and low index layers in top and bottom DBRs at the pump pulses of 20 mJ, 4 ns and the angle of incidence: $\theta_0 = 45°$. (a) for the backward SHG, (b) for the forward SHG. Insert is the reflection spectrum of the MC indicating a defect mode at the wavelength of 0.783 μm.

4. Conclusion

Second harmonic generation in nonlinear photonic crystal microcavities pumped by laser pulses at oblique and normal incidence was discussed. Assuming undepleted-pump approximation, the analytical solutions of the fundamental wave and the second harmonic wave propagation equations could be achieved for the fundamental wave at an arbitrary angle of incidence. Taking into account pump depletion, the solution of the wave propagation equations in one-dimensional photonic crystal microcavities under pump light incidence at an arbitrary angle could be obtained by incorporating the analytical solution of the wave propagation equations in undepleted-pump approximation with the perturbative value generated from pump depletion. The perturbative solution could be found by numerical iteration.

Analysis of the conversion efficiency of second harmonic generation in photonic crystal microcavities indicated that SHG was dramatically enhanced in the MCs with optimal numbers of pairs of Bragg reflectors on both sides of the MCs. High conversion efficiencies of second harmonic generation in the MCs could be achieved. Actually, giant SHG enhancement occurs when pump FWs are located at the defect modes within the forbidden bands of the photonic crystal MCs. In this case, the FWs are in resonance with cavity modes, resulting in very high intensity FW fields confined in the spacer layers of the MCs. Localization of high intensity FW fields enhances the second harmonic generation in the photonic crystal MCs.

Although only second-harmonic generation was discussed, the analytical approach and numerical iteration technique can be applied to study other phenomena such as third-harmonic generation, four-wave mixing, and optical amplification in one-dimensional photonic crystal structures under light incidence at an arbitrary angle.

Acknowledgements

The author is grateful to Prof. Fabrizio Giorgis and Emiliano Descrovi for their help in the work. The author thanks Politecnico di Torino for financial support.